

BiOX (X = Cl, Br, I) nanostructures: Mannitol-mediated microwave synthesis, visible light photocatalytic performance, and Cr(VI) removal capacity

Guangfang Li^a, Fan Qin^a, Runming Wang^a, Shengqiang Xiao^b, Hongzhe Sun^c, Rong Chen^{a,*}

^a Key Laboratory for Green Chemical Process of Ministry of Education and Hubei Novel Reactor & Green Chemical Technology Key Laboratory, Wuhan Institute of Technology, Xiongchu Avenue, Wuhan 430073, PR China

^b State Key Laboratory of Advanced Technology for Materials Synthesis and Processing, Wuhan University of Technology, Wuhan 430073, PR China

^c Department of Chemistry, The University of Hong Kong, Pokfulam Road, Hong Kong Special Administrative Region

ARTICLE INFO

Article history:

Received 17 May 2013

Accepted 31 July 2013

Available online 11 August 2013

Keywords:

BiOX nanostructures

Microwave

Photocatalytic

Cr(VI) removal

ABSTRACT

A facile microwave irradiation method has been successfully developed for the controllable fabrication of BiOX (X = Cl, Br, I) nanostructures in mannitol solution. The morphology and size of BiOX nanostructures could be readily tailored by adjusting the amount of halide, reaction precursor, and mannitol concentration. Mannitol molecule acts as both a capping agent and a cohesive agent in the formation of BiOX nanostructures. A possible two-stage formation mechanism was discussed based on the morphology evolution of BiOI nanostructures obtained in mannitol solution with different concentrations. The as-synthesized BiOX nanostructures exhibit much higher photocatalytic activities than that of commercial TiO₂. In particular, flower-like BiOX hierarchical nanostructures display the best photocatalytic performance, which is mainly ascribed to their unique hierarchical structure, high BET surface area, and large band gap. Moreover, BiOX nanostructures also demonstrate superior Cr(VI) removal capacity. The Cr(VI) adsorption behavior was also analyzed by the Langmuir and Freundlich adsorption isotherms.

© 2013 Elsevier Inc. All rights reserved.

1. Introduction

Contamination of water with organic dyes and heavy metal ions has become a severe environmental problem; thereby, considerable effort has been made to develop advanced methods for water purification [1,2]. As an effective approach, photocatalysis and adsorption have been extensively employed in water treatment, where a variety of advanced nanomaterials have been studied as promising photocatalysts and adsorbents. Bismuth-based nanostructures, in particular, have attracted considerable attention by virtue of their improved properties and extensive applications in removing organic dyes and heavy metal ions [3–7]. During the past few years, an increasing interest has been focused on the fabrication of bismuth-related nanomaterials with tailored morphology and pattern, owing to the strong correlation between the property and performance and their sizes, shapes, and structures [8–14]. For instance, BiOCl nanosheets have been reported to display facet-dependent photoreactivity [15]. Our previous studies also demonstrated that BiOOH and BiPO₄ nanostructures exhibited shape-dependent photocatalytic performances [16,17]. Therefore, systematically controlling the size, shape, and structure of

bismuth-based nanomaterials represent an alternative approach, which may open up new possibilities to improve their fascinating properties as well as potential functions.

Among mostly reported bismuth-based nanostructures, bismuth oxyhalide (BiOX, X = Cl, Br, I) nanomaterials are of special interest due to their promising applications in environmental remediation. BiOX has been viewed as a new kind of novel photocatalysts for NO oxidation, organic pollutants degradation, and sterilization [18–23]. Apart from this, BiOX nanostructures also demonstrate effective removal capacity for heavy metal ions and organic dyes [24,25]. Until now, different BiOX micro/nanostructures have been successfully synthesized by utilizing hydro-/solvo-thermal [18,26], chemical vapor transport [27], reverse microemulsions [28], and sonochemical methods [29], which usually involved extremely high temperature, long reaction time, sharp thermal gradients, and hard-control process. Few works have achieved to the controlled synthesis of BiOX nanostructures through facile and environment-friendly approaches. Currently, microwave irradiation method has been considered as a facile, rapid, and mild technique for the fabrication of diverse nanomaterials with controllable shape and size [30–35]. It offers great advantages of uniform and rapid dielectric heating without thermal gradient effects, which dramatically promotes the reaction rate and leads to a high throughput capacity and reproducibility of nanostructures.

* Corresponding author. Fax: +86 2787195671.

E-mail address: rchenku@hotmail.com (R. Chen).

In this work, a facile microwave irradiation method was employed for synthesis of BiOX nanostructures in mannitol solution. By varying appropriate experimental parameters, such as the amount of halide, reaction precursor, and mannitol concentration, BiOX nanostructures with different sizes and morphologies have been successfully fabricated. Moreover, the photocatalytic performance of the BiOX nanostructures was evaluated by the degradation of RhB under visible light irradiation, and their adsorptive capacities for heavy metal ions were also investigated. To the best of our knowledge, systematic investigation of mannitol-assisted fabrication of BiOX nanostructures and their heavy metal ions removal capacities have seldom reported.

2. Experimental

2.1. Chemicals

Bismuth nitrate pentahydrate ($\text{Bi}(\text{NO}_3)_3 \cdot 5\text{H}_2\text{O}$) was purchased from Tianjin Fuchen chemical reagents factory of China. Sodium chloride (NaCl) and mannitol were purchased from Sinopharm chemical reagent Co., Ltd. (Shanghai, China). Potassium bromide (KBr), potassium iodide (KI), Rhodamine B (RhB), cetyltrimethylammonium bromide (CTAB), and potassium bichromate ($\text{K}_2\text{Cr}_2\text{O}_7$) were purchased from Aladdin (Shanghai, China). All the reagents are of analytical grade and used directly without further purification.

2.2. Synthesis

In a typical synthesis, 0.485 g (1 mmol) bismuth nitride ($\text{Bi}(\text{NO}_3)_3 \cdot 5\text{H}_2\text{O}$) was dissolved into 30 mL mannitol solution (0.1 M), which contained 0.058 g NaCl (1 mmol). After sonication for several minutes, the mixture was heated to 110 °C within 3 min and then kept at this temperature for 27 min by a microwave reactor with a microwave irradiation power of 500 W (XH-300A, Beijing Xianghu Technology Co., Ltd.). After microwave treatment, the mixture was cooled down to room temperature naturally. A white precipitate was collected by centrifugation and washed with deionized water and ethanol for six times. Finally, the product was dried in a desiccator for a few days for further characterization (**SC1**). Other BiOX samples were also prepared under identical conditions by changing the amount of halide, reaction precursor (KBr, KI, CTAC, CTAB), and mannitol concentration. The detailed experimental parameters are listed in Table 1.

2.3. Characterizations

Powder X-ray diffraction (XRD) was carried out on Bruker axS D8 Discover ($\text{Cu K}\alpha = 1.5406 \text{ \AA}$) at a scan rate of 2° min^{-1} in the 2θ range from 10° to 70° . Scanning electron microscopy (SEM) images were taken on a Hitachi S4800 scanning electron microscope operating at 5.0 kV. Transmission electron microscopy (TEM) images selected area electron diffraction (SAED) patterns were recorded on a Philips Tecnai G2 20 electron microscope, using an accelerating voltage of 200 kV. UV–vis diffuse reflectance spectra (DRS) were recorded on a UV–vis spectrometer (Shimadzu UV-2550) by using BaSO_4 as a reference. Brunauer–Emmett–Teller (BET) surface area and pore-size distribution were analyzed by nitrogen adsorption (Micromeritics ASAP 2020). All the products were degassed at 100 °C for 4 h prior to the measurement.

2.4. Photocatalytic test

The photocatalytic activities of the synthesized BiOX samples were evaluated by the degradation of RhB under visible light irradiation.

Table 1

Experimental conditions for the preparation of BiOX nanostructures^a.

Sample	Halogen precursor	Amount (mmol) ^b	Solvent
SC1/SB1/SI1	NaCl/KBr/KI	1/1/1	0.1/0.1/0.1 M mannitol
SC2/SB2/SI2	NaCl/KBr/KI	2/2/2	0.1/0.1/0.1 M mannitol
SC3/SB3/SI3	NaCl/KBr/KI	4/4/4	0.1/0.1/0.1 M mannitol
SC4/SB4/SI4	CTAC/CTAB/KI	0.1/0.1/1	0.1/0.1/0.05 M mannitol
SC5/SB5/SI5	NaCl/KBr/KI	1/1/1	0.05/0.05/0.3 M mannitol
SC6/SB6/SI6	NaCl/KBr/KI	1/1/1	0.6/0.6/0.6 M mannitol
SC7/SB7/SI7	NaCl/KBr/KI	1/1/1	$\text{H}_2\text{O}/\text{H}_2\text{O}/\text{H}_2\text{O}$
SC8/SB8	CTAC/CTAB	0.1/0.1	$\text{H}_2\text{O}/\text{H}_2\text{O}$

^a The bismuth precursor for all the reactions was $\text{Bi}(\text{NO}_3)_3 \cdot 5\text{H}_2\text{O}$ (1 mmol).

^b The amount of halogen precursor (mmol).

In the experiment, 0.01 g BiOX sample was added into 100 mL RhB aqueous solution ($1 \times 10^{-5} \text{ mol L}^{-1}$) at room temperature. Prior to irradiation, the solution was stirred for 30 min in dark to ensure the establishment of an adsorption–desorption equilibrium. Then, the solution was exposed to 500 W Xe lamp light irradiation with a 400 nm cutoff filter under magnetic stirring. At each given time interval, 3 mL suspension was sampled and centrifuged to remove the BiOX powder. The concentration variation in RhB was analyzed by a Shimadzu UV2800 UV–vis spectrophotometer, and the characteristic absorption of RhB at 554 nm was used to monitor the RhB concentration. As a comparison, blank experiments were also conducted in the absence of BiOX products under the same condition.

2.5. Cr(VI) removal experiments

The initial Cr(VI) solution was prepared by dissolving $\text{K}_2\text{Cr}_2\text{O}_7$ in deionized water at room temperature. BiOX product (20 mg) was added to 20 mL prepared $\text{K}_2\text{Cr}_2\text{O}_7$ solution ($10\text{--}60 \text{ mg L}^{-1}$) with constant stirring. At each given time interval, 2 mL suspension was sampled and centrifuged to remove the BiOX powder. The concentration variation in Cr(VI) was analyzed by a Shimadzu UV2800 spectrophotometer, and the characteristic absorption of Cr(VI) at around 354 nm was used to monitor the Cr(VI) concentration.

3. Results and discussion

3.1. Structure and morphology

The phase and purity of the products (**SC1**, **SB1**, and **SI1**) were identified by the XRD patterns. As shown in Fig. S1 (Supporting Information), BiOCl, BiOBr, and BiOI products could be obtained by microwave irradiation in 0.1 M mannitol solution which contained 1 mmol NaCl, KBr, and KI, respectively (**SC1**, **SB1**, and **SI1**). All the diffraction peaks were labeled and could be readily indexed to tetragonal phase of BiOCl (JCPDS 73-2060), BiOBr (JCPDS 73-2061), and BiOI (JCPDS 73-2062), respectively. No impurity peak was detected, indicative of the high purity of BiOX products. The intense and sharp diffraction peaks suggest that the as-synthesized products were well-crystallized.

The morphologies and structures of the as-synthesized BiOX products (**SC1**, **SB1** and **SI1**) were characterized by SEM and TEM images, as shown in Fig. 1. Typical SEM and TEM images of sample **SC1** show that the BiOCl product is composed of a large quantity of nanoparticles with a narrow size distribution from 10 to 15 nm

(Fig. 1a and b). The corresponding selected area electron diffraction (SAED) pattern in Fig. 1c clearly demonstrates a high polycrystalline nature of BiOCl nanoparticles. Fig. 1d and e reveal the fabrication of BiOBr nanoparticles with average diameter of 20 nm (SB1). As depicted in Fig. 1g and h, irregular BiOI nanoplates with the thickness of 10 nm were formed, whose diameters range from 40 to 100 nm (SI1). SAED patterns in Fig. 1f and i also demonstrate polycrystalline structures of the as-prepared BiOBr and BiOI nanostructures (SB1 and SI1), respectively.

3.2. Influence of the amount of halide

The influence of the halide concentration on the formation of BiOX nanostructures was investigated. It was obviously found that the variation in halide concentration resulted in a distinctive difference in the morphology and size of BiOX nanostructure. Fig. 2a–d show the SEM and TEM images of BiOCl nanostructures prepared in the presence of different amounts of NaCl. In presence of 2 mmol NaCl, the BiOCl product (SC2) consists of well-defined nanosheets (ca. 30 nm in width), as depicted in Fig. 2a and b. Further increasing NaCl amount to 4 mmol, uniform BiOCl nanoplates about 10 nm in the thickness and 60 nm in width were fabricated (SC3, Fig. 2c and d). The SEM and TEM images of BiOBr products prepared from various KBr concentrations are shown in Fig. 2e–h. Uniform square nanosheets (ca. 40 nm in width) were fabricated in the presence of 2 mmol KBr (SB2, Fig. 2e and f). When KBr amount was 4 mmol, relatively large BiOBr nanoplates with width of 60 nm and thickness of 10 nm were obtained, as displayed in Fig. 2g and h (SB3). BiOI nanostructures with different sizes and thicknesses were also prepared from different amounts of KI. It clearly manifests that BiOI nanoplates (ca. 70–130 nm in width and 20 nm in thickness, SI2) and irregular microsheets (ca. 50 nm in thickness, SI3) were obtained in the presence of 2 or 4 mmol

KI, respectively (Fig. 2i–l). The results indicate that the morphologies of BiOX nanostructures changed with the concentration of halide. At the same time, the average crystal size of BiOX product increased with the increase in the halide concentration, which also could be verified by the variation in the XRD patterns of BiOX products, obtained under different halide concentrations (Fig. S2, Supporting Information). The characteristic diffraction peaks of BiOX nanostructures prepared under lower halide concentration were remarkably broadened, suggesting the fabrication of BiOX nanostructures with smaller particle size.

3.3. Influence of reaction precursor

In this work, the influence of halide precursor on the fabrication of BiOX nanostructures was also investigated. Instead of NaCl and KBr, CTAC and CTAB were used as halide precursors to synthesize BiOCl and BiOBr nanostructures under the similar conditions (SC4 and SB4). The corresponding XRD patterns illustrate that BiOCl and BiOBr were also successfully obtained (Fig. S3, Supporting Information). The broad diffraction peaks might be ascribed to small crystal size, lower crystallinity, microstrain effects. However, the morphologies of SC4 and SB4 varied significantly from that of the products obtained from NaCl and KBr. SEM images of SC4 and SB4 in Fig. 3a and d demonstrate that the samples are composed of a large quantity of uniform flower-like hierarchical nanostructures with a diameter of 200–300 nm. Fig. 3b and e further provide the detailed structure information of the flower-like nanostructures. It shows that the hierarchical nanostructure is built up from a series of thin nanosheets, which are loosely packed and connect to each other through the center to form flower-like nanostructures. The high-magnification TEM images (Fig. 3c and f) clearly reveal that the nanosheet is constructed by many small nanoparticles, which could well explain the broadening of XRD

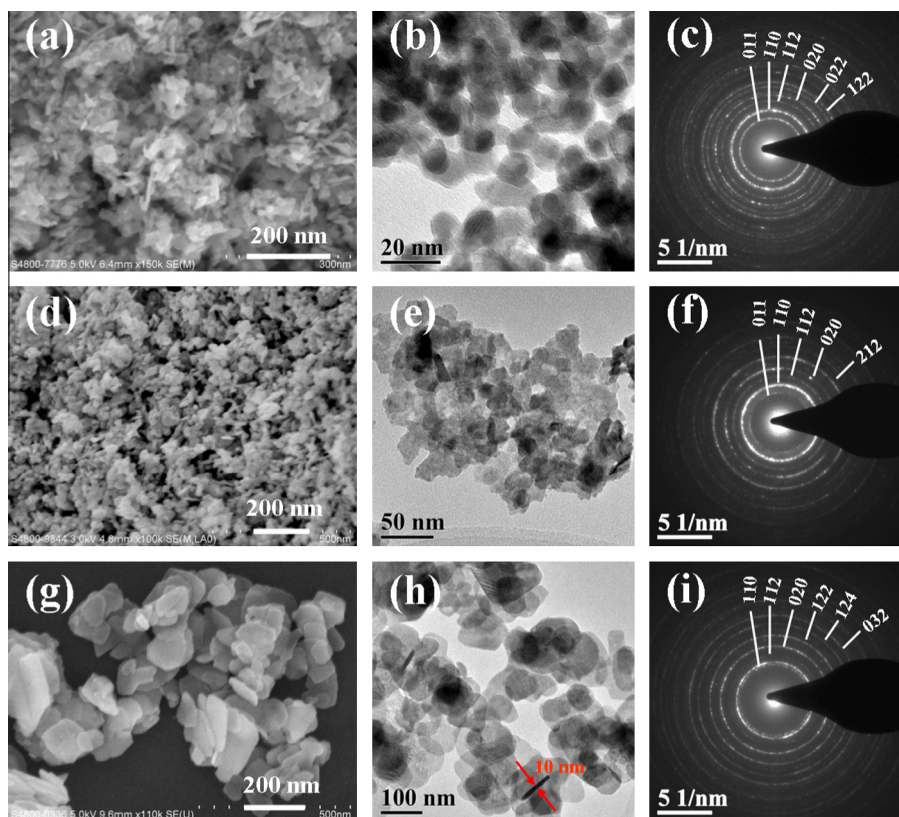


Fig. 1. SEM, TEM images, and SAED patterns of BiOX nanostructures synthesized in 0.1 M mannitol solution: (a–c) BiOCl, SC1; (d–f) BiOBr, SB1; (g–i) BiOI, SI1.

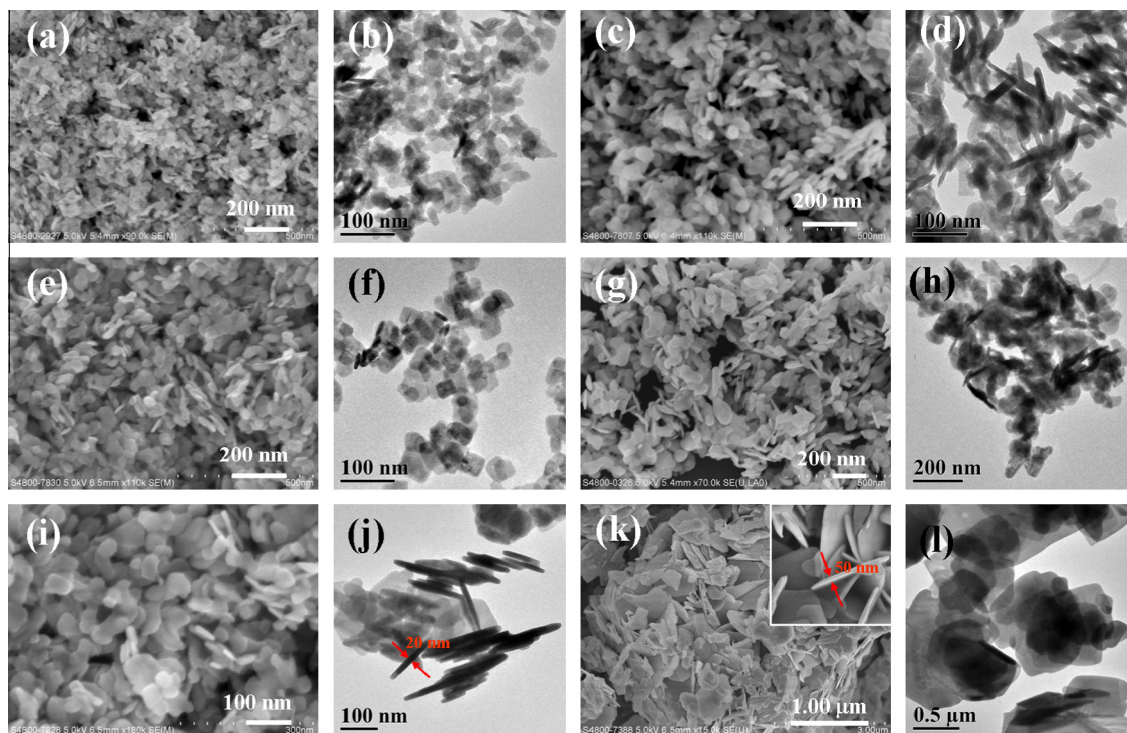


Fig. 2. SEM and TEM images of BiOX nanostructures synthesized in 0.1 M mannitol solution in the presence of different amounts of halide: (a and b) **SC2**; (c and d) **SC3**; (e and f) **SB2**; (g and h) **SB3**; (i and j) **SI2**; (k and l) **SI3**.

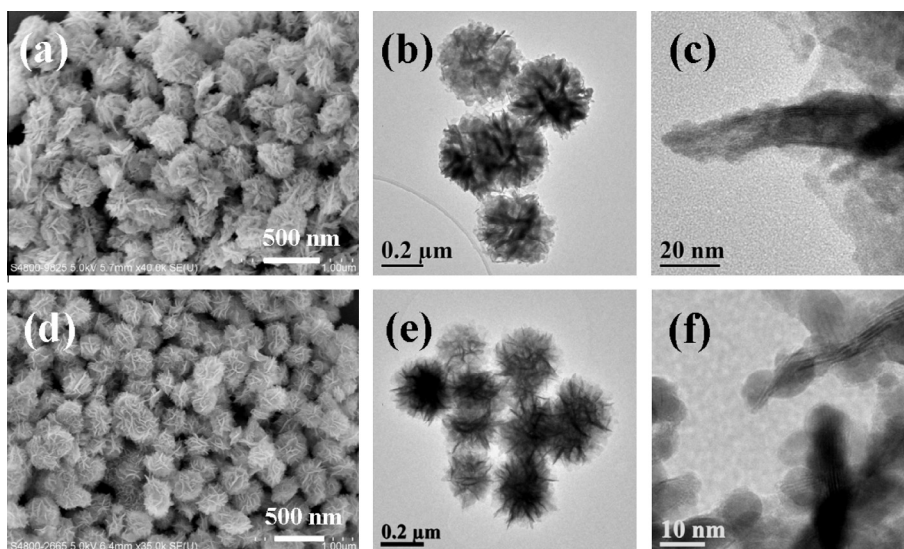


Fig. 3. SEM and TEM images of BiOCl (a–c, **SC4**) and BiOBr (d–f, **SB4**) nanostructures synthesized from CTAC and CTAB in 0.1 M mannitol solution.

diffraction peaks. Based on the results, it is believed that CTAC and CTAB serve as not only the halogen resource but also the soft template, which facilitates the assembly of nanosheets into flower-like hierarchical nanostructures through the interaction between CTA^+ ions and the petals. It was also reported in the fabrication of flower-like CeO_2 and BaMoO_4 hierarchical nanostructures [36,37]. Under the same condition, deionized water was employed as solvent instead of mannitol solution, and bulk agglomeration consisted of large crystals was generated (Fig. S4, Supporting Information), which illustrated that the mannitol also played a critical function in the formation of BiOCl and BiOBr flower-like nanostructures.

3.4. Function of mannitol

In order to gain insight into the function of mannitol, the equivalent volume of deionized water was used, instead of mannitol solution to prepare BiOX nanostructures under identical conditions (**SC7**, **SB7**, and **SI7**). BiOX products also could be obtained in pure water, as confirmed by the corresponding XRD patterns (Fig. S5, Supporting Information). However, remarkable difference in the relative intensity of diffraction peaks could be observed. Taking BiOCl as an example, BiOCl crystal has a layered structure characterized by $[\text{Bi}_2\text{O}_2]$ slabs which are interleaved by double slabs of Cl atoms, and the dominant facets of BiOCl crystal are (001) and

(110) (Fig. S6, Supporting Information) [38]. In the standard database of BiOCl (JCPDS 73-2060), the relative peak intensity corresponding to $I(001)/I(110)$ planes is 1.15. The value of $I(001)/I(110)$ in the XRD pattern of BiOCl product (SC7) prepared in H₂O is 5.27, indicating that BiOCl favors to grow along the c axis ([001] orientation) perpendicular to the platelets (Fig. S6d) [39,40]. However, the relative intensity of (001) and (110) planes is only 0.16 in the XRD pattern of SC1 obtained in 0.1 M mannitol, suggesting that the mannitol restricted the crystal anisotropic growth along the [001] direction and thus led to relatively weak intensity of (001) plane. This speculation was further confirmed by the decline of $I(001)/I(110)$ value of the BiOCl nanostructures (SC5, SC1, and SC6) with the increase in mannitol concentration (Table S1, and Fig. S7a in Supporting Information). It was also found that the half width of the (001) XRD peak of sample SC5, SC1, and SC6 increased with the increase in mannitol concentration (Fig. S7b, Supporting Information), indicating the increase in thickness $d_{(001)}$ of the BiOCl products and the corresponding crystallite size. Noticeably, the similar variation tendency of $I(001)/I(110)$ and $I(004)/I(110)$ was also observed in the XRD patterns of BiOBr and BiOI nanostructures prepared in the presence of different mannitol concentrations (Table S1, Fig. S8 in Supporting Information). In addition, SEM images reveal that irregularly bulky and thick BiOX microplates with a wide size distribution were obtained in deionized water (SC7, SB7, and S17), which also illustrates the fast anisotropic growth rate in the absence of mannitol (Fig. S9, Supporting Information).

The experiments also revealed that the morphologies of BiOX were intensely dependent on the concentration of mannitol. Fig. 4 shows the SEM and TEM images of BiOI nanostructures prepared in mannitol solution with different concentrations. In 0.05 M mannitol solution, irregular BiOI nanosheets with a wide size distribution (20–150 nm in width) were fabricated (S14, Fig. 4a and b). As mentioned above, uniform BiOI nanoplates were obtained in 0.1 M mannitol solution (S11, Fig. 1g and h). When the mannitol solution was 0.3 M, flower-like hierarchical BiOI nanostructures consisted of comparatively regular nanoplates were formed (S15, Fig. 4c and d). With further increasing mannitol concentration to 0.6 M, well-defined flower-like hierarchical nanostructures with a uniform diameter about 700 nm were fabricated as a dominant morphology (S16), as depicted in Fig. 4e and f. The results illustrate that the morphology of BiOI changed dramatically with the variation in mannitol concentrations, and uniform 3D hierarchical nanostructures could also be formed by modulating the mannitol concentration. The similar morphology transformation was also observed in the preparation of BiOBr (Fig. S10, Supporting Information); with the increasing of the concentration of mannitol, hierarchical BiOBr nanostructures consisted of nanoparticles were obtained. For the fabrication of BiOCl, however, only nanoparticles with diameters of several nanometers were observed in high concentration mannitol solution (Fig. S10). The failure to obtain hierarchical crystals might be ascribed to the weak interaction force between mannitol and smaller BiOCl particles.

In the literature, it was reported that ethylene glycol molecules could easily generate long chains due to the effect of hydrogen bonds and then induce the formation of hierarchical structures [18]. Considering the six hydroxyl groups, it was also believed that mannitol molecules played a critical role in the formation of BiOX nanostructures. Together with the experimental results, it is proposed that mannitol might serve as both a capping agent and a cohesive agent during the formation of BiOX nanostructures. A possible two-stage formation process of BiOI nanostructures in different mannitol concentrations was speculated. In the initial stage, mannitol molecules directed tiny BiOI nuclei to growing into special nanoplates or nanoparticles as capping agents. With the proceeding of the reaction, adequate mannitol molecules work as

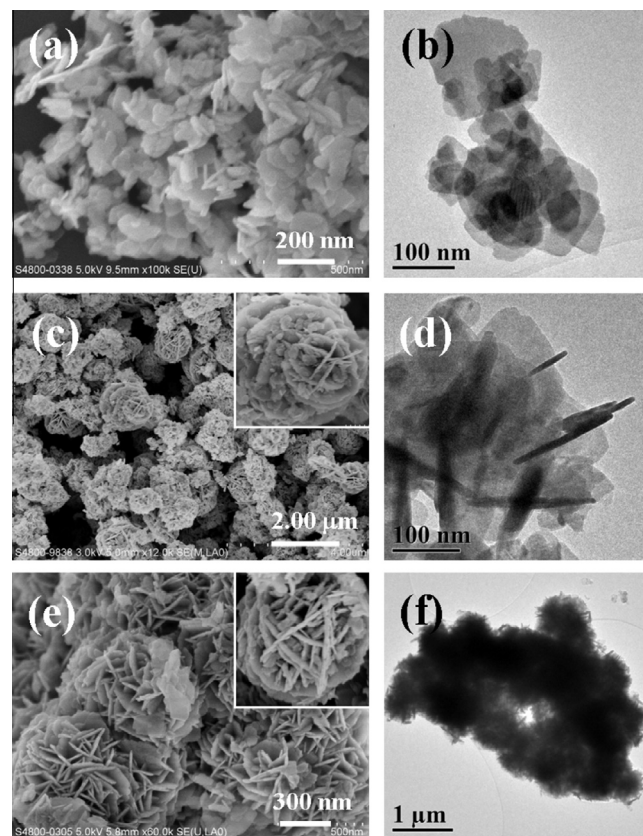


Fig. 4. SEM and TEM images of BiOI nanostructures synthesized in mannitol solution with different concentrations (a and b, 0.05 M, S14; c and d, 0.3 M, S15; e and f, 0.6 M, S16).

cohesive agents to prompt the assembly of 3D hierarchical structures consisted of nanoplates or nanoparticles. However, our understanding is still pretty limited, and further investigation is needed in our further work.

3.5. Optical property and BET surface area

The optical properties of the as-prepared different BiOX nanostructures were measured by UV–visible diffuse reflectance spectra (DRS). Fig. 5 shows the DRS spectra of the as-prepared BiOCl (SC2–SC4), BiOBr (SB2–SB4), and BiOI (S11–S13 and S16) nanostructures. The DRS spectra of BiOCl nanostructures (SC2–SC4) are illustrated in Fig. 5a. All BiOCl products present the photoabsorption mainly in UV light region. The steep shape of the visible absorption band is probably due to the intrinsic transition between the valence band and the conduction band [41]. As a crystalline semiconductor, it is well known that the optical absorption near the band edge follows the formula: $\alpha hv = A(hv - E_g)^n$, where α , h , v , A , E_g are absorption coefficient, plank constant, light frequency, proportional constant, and band gap energy and n is 4 for indirect transition [42]. Plotting $(\alpha hv)^{1/2}$ versus photon hv based on the spectral response in Fig. 5b gave the extrapolated intercept corresponding to the E_g value. The band gap of BiOCl nanostructures (SC2–SC4) is 3.05, 3.01, and 3.09 eV, respectively. Fig. 5c shows that BiOBr products display strong photoabsorption property from UV light to visible light region. Compared with BiOBr nanosheets (SB2) and nanoplates (SB3), obvious blueshift appears in the DRS spectrum of flower-like BiOBr nanostructures (SB4), which probably results from the quantum size effect [43]. According to the same calculation method mentioned above, the estimated band gap of different BiOBr nanostructures (SB2–SB4) is about 2.52, 2.46, and 2.70 eV, respectively

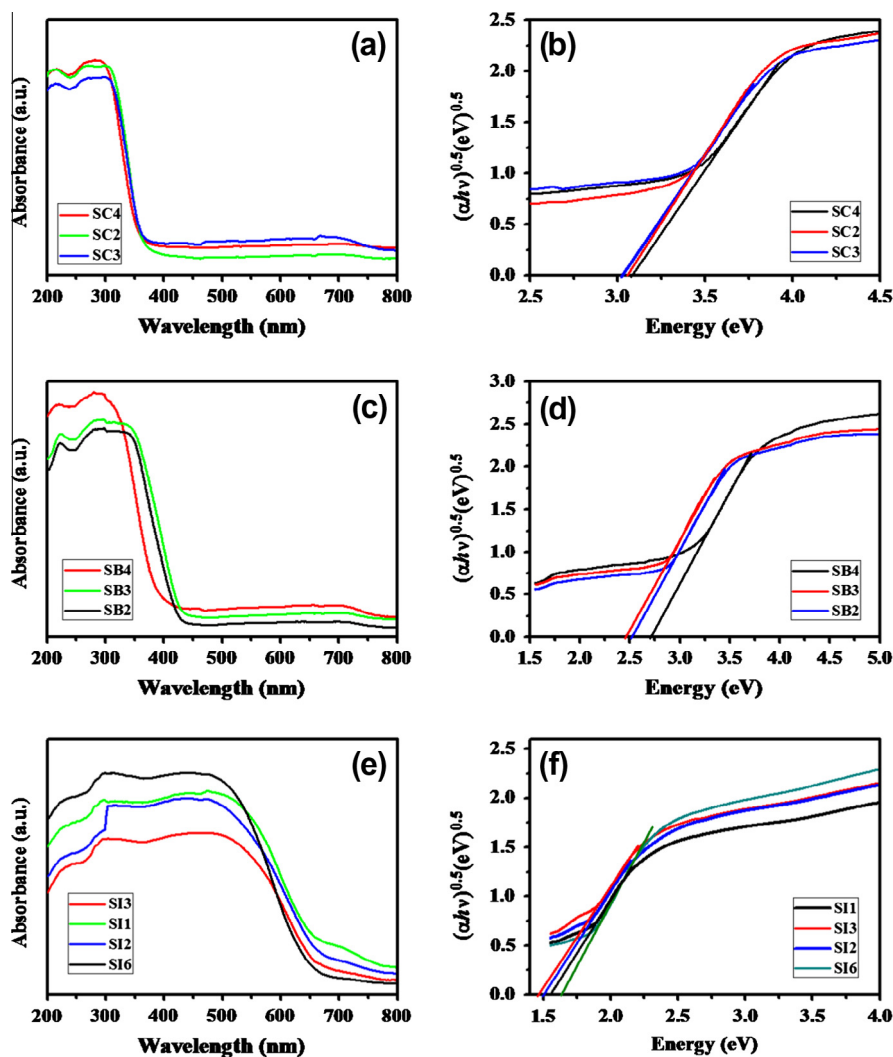


Fig. 5. UV-vis diffuse reflectance spectra and the $(\alpha h\nu)^{1/2}$ versus photon energy ($h\nu$) curve of the different BiOCl (a–b, **SC2–SC4**), BiOBr (c–d, **SB2–SB4**) and BiOI nanostructures (e–f, **SI1–SI3, SI6**), respectively.

(Fig. 5d). As shown in Fig. 5e, BiOI products (**SI1–SI3, SI6**) display strong photoabsorption performance in visible light region. The band gap of different BiOI nanostructures (**SI1–SI3** and **SI6**) is 1.55, 1.50, 1.46, and 1.63 eV, respectively (Fig. 5f). It clearly demonstrates that the band gap of different BiOX ($X = \text{Cl, Br, and I}$) nanostructures varies slightly and increases with the decrease in crystal size. Summary of band gap and crystal size for BiOX nanostructures was listed in Table 2. The variations in the band gap could lead to different degrees of delocalization, recombination, and mobility of photo-induced electron-hole pairs, which may also contribute to different photocatalytic efficiencies.

It is widely accepted that the surface area of photocatalyst or adsorbent has exerted a noticeable influence on its catalytic activity or adsorptive capacity. Hence, the BET surface areas of the BiOX nanostructures (**SC2–SC4, SB2–SB4, SI1–SI3, and SI6**) were investigated by nitrogen adsorption and desorption isotherms (Fig. S11–S13, Supporting Information). All of them display type IV isotherm with a type H3 hysteresis loop at high relative pressures between 0.8 and 1.0, flower-like hierarchical BiOX nanostructures (**SC4, SB4, and SI6**) show a distinct hysteresis loop in the range of 0.5–1.0 p/p_0 , and the loop shifts approach $p/p_0 \approx 1$, indicating the presence of mesopores and macropores [41,44]. Both mesopores and macropores up to 100 nm could be observed in corresponding pore-size distributions (insets of Fig. S11–S13, Supporting Information).

Table 2

Summary of crystal size and band gap for BiOX nanostructures.

Sample	Halogen precursor	Crystal size (nm) ^a	Band gap (eV)
SC2/SC3/SC4	NaCl/NaCl/CTAC	30/60/10	2.52/2.46/2.70
SB2/SB3/SB4	KBr/KBr/CTAB	40/60/10	3.05/3.01/3.09
SI1/SI2/SI3/SI6	KI/KI/KI/KI	10/20/50/10	1.55/1.50/1.46/1.63

^a The average size or thickness of structural units of BiOX nanostructures.

The small pores might be generated during the crystal growth process and the large ones probably result from the space between the intercrossed BiOX nanosheets or petals [45]. The specific surface areas of BiOX nanostructures (**SC2–SC4, SB2–SB4, SI1–SI3, and SI6**) calculated from the results of N_2 adsorption isotherms are summarized in Table S2 (Supporting Information).

3.6. Photocatalytic activity

Photocatalytic activities of the as-synthesized different BiOX nanostructures were evaluated by the RhB degradation under visible light irradiation. For comparison, direct RhB photolysis and RhB degradation over commercial TiO_2 were also performed under

identical conditions. Fig. 6a shows the variation in RhB concentration (C/C_0) with irradiation time over different BiOBr nanostructures (SB2–SB4), where C_0 is the initial concentration of RhB and C is the RhB concentration at t time. It is clearly observed that RhB concentration hardly changed with the increase in irradiation time in the absence of BiOBr, and the photodegradation efficiency of BiOBr nanostructures (SB2–SB4) is significantly higher than that of commercial TiO_2 , which only decomposed about 5% of RhB after 25 min visible light irradiation. Among them, flower-like hierarchical nanostructure (SB4) exhibits the highest photocatalytic activity. Fig. 6b displays the photodegradation efficiency of RhB in the presence of different BiOCl nanostructures (SC2–SC4) upon visible light irradiation. All BiOCl nanostructures demonstrate improved photocatalytic performance compared with commercial TiO_2 , and flower-like BiOCl nanostructures (SC4) also exhibit the best photocatalytic activity. In theory, BiOCl mainly absorbs the UV light based on its UV–vis diffuse reflectance edges. Hence, the RhB degradation over BiOCl nanostructures upon visible light irradiation might proceed in a photosensitization pathway, which was reported in our previous work [21]. Fig. 6c displays the variation in RhB concentration (C/C_0) versus time over different BiOI nanostructures (SI1–SI4 and SI6). All the BiOI nanostructures also possess good photocatalytic activities. Besides, it is also worth mentioning that BiOX nanostructures exhibited strong adsorptive capacity of RhB in dark, especially for flower-like BiOX nanostructures. Nearly 50% RhB was adsorbed by flower-like BiOCl and BiOBr nanostructures, and flower-like BiOI hierarchical nanostructures (SI6) even could completely adsorb RhB dye molecules within 20 min (Fig. 6d). However, the adsorbed RhB molecules could not be degraded in dark. Contrarily, under visible light irradiation, all the adsorbed RhB could be completely decomposed, which could be verified by the color variation and IR spectra of the product collected before and after adsorption and photocatalysis (Fig. S14, Supporting Information). The excellent photocatalytic performance of flower-like BiOX hierarchical nanostructures could be attributed to their specific structure, large band gap, high surface area, and strong adsorptive ability, which are the key factors for the

enhancement of photocatalytic activity. In particular, the hierarchical nanostructures could greatly enhance availability of the injected photons; the ultrathin petals of the flower-like nanostructures promote charge carriers to move rapidly from the interior to the surface to participate in the photocatalytic reaction; and the wide band gap also could slow electron hole recombination rate [46]. The large specific surface area, on the other hand, could provide more catalytic sites and harvest light efficiently during the photocatalytic process [47]. Their excellent visible light-driven activities should be significantly valuable for further practical application in water treatment.

3.7. Cr(VI) removal capacity

Chromium(VI) is considered as primary highly toxic pollutants in water, and its efficient removal is of considerable significance. Inspired by the superior dye adsorption ability of BiOX nanostructures, the Cr(VI) removal capacities of the as-synthesized BiOX nanostructures (SC2–SC4, SB2–SB4, SI1–SI3, and SI6) were also investigated. Fig. 7a–c represent the time-dependent Cr(VI) concentration variation curve over different BiOBr (SB2–SB4), BiOCl (SC2–SC4), and BiOI (SI1–SI3 and SI6) nanostructures with an initial $\text{K}_2\text{Cr}_2\text{O}_7$ concentration of 60 mg L^{-1} , respectively. Compared with commercial TiO_2 , all the samples demonstrate highly efficient Cr(VI) adsorptive capacities, indicating that the as-prepared BiOX nanomaterials could be used as potential adsorbents for heavy metal ions removal, especially for the flower-like BiOX nanostructures (SB4, SC4, and SI6). It is also observed that the adsorption rates were considerably fast in the initial 15 min from the time-dependent optical absorption spectra of $\text{K}_2\text{Cr}_2\text{O}_7$ solution (Fig. S15, Supporting Information). The measured Cr(VI) removal capacities of the as-obtained BiOX nanostructures (SB2–SB4, SC2–SC4, SI1–SI3, and SI6) with an initial Cr(VI) concentration of 60 mg L^{-1} are summarized in Table S3 (Supporting Information). Flower-like hierarchical BiOX nanostructures (SB4, SC4, and SI6) exhibited much higher Cr(VI) removal ability than that of other BiOX nanostructures, which could be ascribed to their unique hierarchical

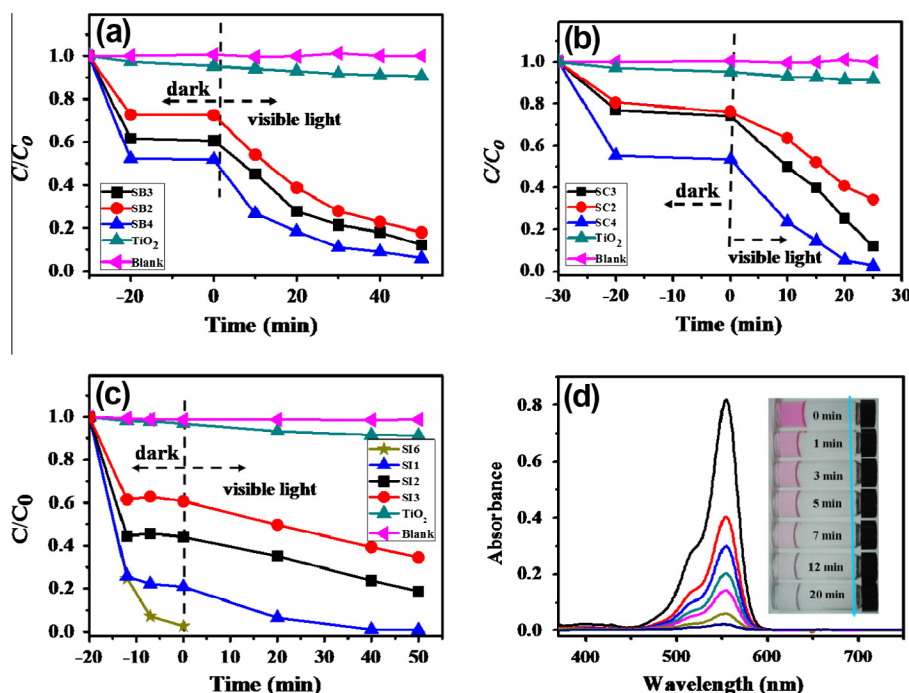


Fig. 6. Dark adsorption and visible light-induced photocatalytic degradation of RhB over BiOX nanostructures (a, SB2–SB4; b, SC2–SC4; c, SI1–SI3 and SI6) and UV–visible spectra (d) and photographic images (inset of Fig. 6d) of RhB solution during adsorption process in the presence of flower-like BiOI nanostructures in dark (d, SI6).

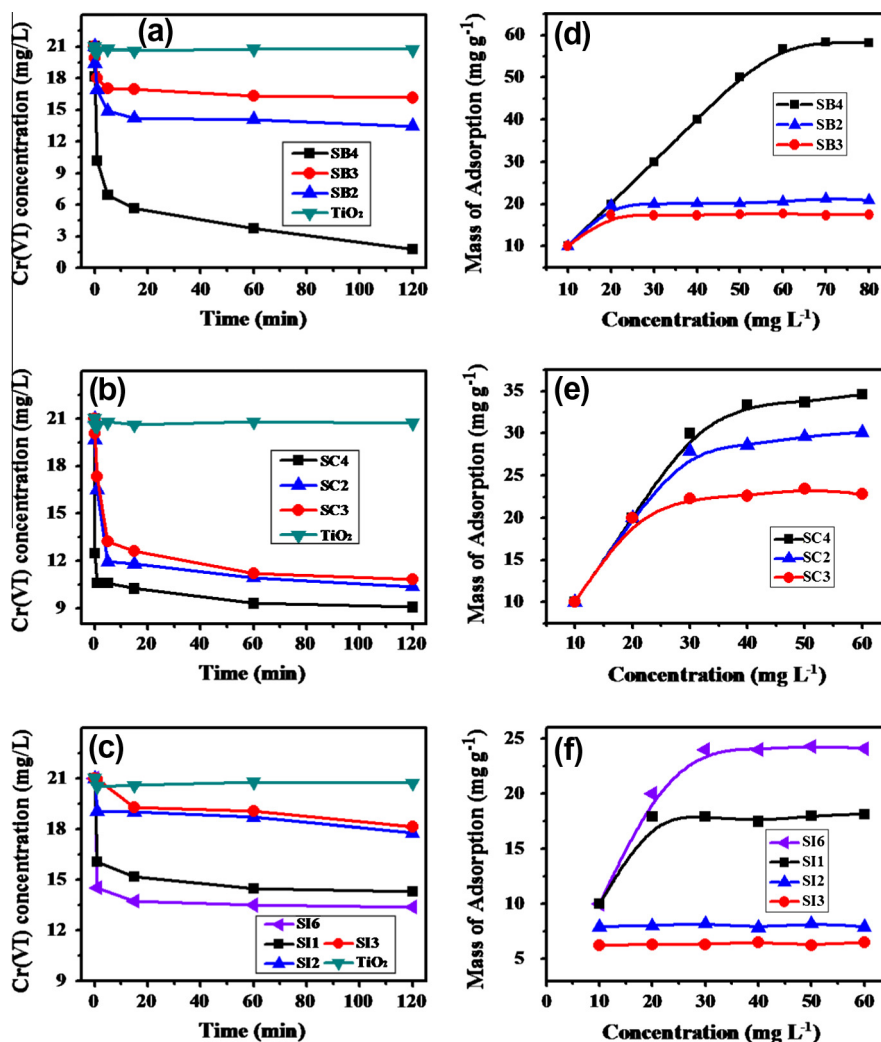


Fig. 7. Time-dependent Cr(VI) concentration variation curve (a–c) and adsorption isotherms (d–f) over BiOX nanostructures (a and d, BiOBr; b and e, BiOCl; c and f, BiOI).

structures and relatively large specific surface areas. However, flower-like BiOI nanostructures with remarkable RhB adsorptive capacity show relatively lower Cr(VI) removal efficiency compared with BiOBr and BiOCl flower-like nanostructures, which might be strongly associated with their different intrinsic properties such as distribution of surface charge, isoelectric point, BET surface area, working pH, and so on. In this work, the higher RhB adsorptive capacity of flower-like BiOI nanostructures (SI6) is probably owing to its more negative isoelectric point (IEP). The IEP of flower-like BiOBr (SB4), BiOCl (SC4), and BiOI (SI6) nanostructures was estimated approximately to be 2.6, 1.9, and 0.9 (Fig. S16, Supporting Information), indicating that flower-like BiOI nanostructures produce more negatively charged species in RhB aqueous solution, which led to higher adsorption capacity of positively charged RhB ions on BiOI [48]. In contrast, the relatively positive isoelectric point and large BET surface of flower-like BiOBr nanostructures might significantly contribute to its outstanding removal capacity of negatively Cr(VI) species in water solution. However, the in-depth investigation like effect of working pH is still needed in our future work.

The adsorption isotherms of Cr(VI) on BiOX nanostructures (SC2–SC4, SB2–SB4, SI1–SI3, and SI6) were also measured under different initial Cr(VI) concentrations, as illustrated in Fig. 7d–f. It represents the relationship between the amount of adsorbed Cr(VI) ions (q_e , mg g^{-1}) and Cr(VI) initial concentration (C_e , mg L^{-1}) at equilibrium on different BiOX nanostructures. In order to under-

stand the Cr(VI) removal behavior, the Langmuir and Freundlich adsorption models were used to analyze the adsorption equilibrium isotherms (Fig. S17, Supporting Information). Taking BiOBr nanostructures as an example, the estimated model parameters together with correlation coefficient (R^2) for the different models are summarized in Table S4 (Supporting Information). It indicates that the Langmuir model fits the adsorption data better than the Freundlich model for BiOBr nanostructures (SB2–SB4), suggesting the monolayer adsorption of Cr(VI) ions on the surface of BiOBr nanostructures [49]. The maximum Cr(VI) adsorption capacity (q_{max}) of the BiOBr nanostructures (SB2–SB4) were estimated to be 20.7, 17.7, and 63.5 mg g^{-1} , respectively. The Cr(VI) adsorption behavior of BiOCl and BiOI nanostructures was also analyzed by the same method, and the corresponding maximum Cr(VI) adsorption capacity (q_{max}) is listed in Table 3. Compared with most reported adsorbents [50–53], the obtained BiOX nanostructures possess much higher Cr(VI) removal capacities, indicating that it is potential to become promising adsorbent in the purification of chromium industrial wastewater.

4. Conclusion

In summary, BiOX (X = Cl, Br, I) nanostructures have been successfully synthesized via a facile and rapid microwave irradiation method in mannitol solution. The sizes, morphologies, and struc-

Table 3

The maximal Cr(VI) removal capacities of the as-synthesized BiOX nanostructures.

BiOBr		BiOCl		BiOI	
Sample	Removal capacity (mg g ⁻¹)	Sample	Removal capacity (mg g ⁻¹)	Sample	Removal capacity (mg g ⁻¹)
SB2	20.7	SC2	32.8	SI1	18.2
SB3	17.7	SC3	23.7	SI2	8.2
SB4	63.5	SC4	40.1	SI3	6.5
				SI6	26.4

tures of BiOX nanostructures could be easily controlled by varying the amount of halide, reaction precursor, and mannitol concentration. Mannitol plays a critical role in the modulating, the formation and assembly of BiOX nanostructures, which serves as not only a capping agent but also a cohesive agent. A possible two-stage formation mechanism was discussed based on the morphology evolution of BiOI nanostructures under different mannitol concentrations. The obtained BiOX nanostructures exhibit shape-associated improved photocatalytic performance for RhB degradation under visible light irradiation. Flower-like BiOX hierarchical nanostructures show the highest photocatalytic activity, which is mainly ascribed to their unique hierarchical structure, wide band gap, and large BET surface area. In addition, the as-synthesized BiOX nanostructures also exhibit remarkable Cr(VI) removal capacities. This work not only demonstrates a facile and fast pathway to fabricate BiOX nanostructures, but also provides a new approach for the controllable synthesis of bismuth-containing nanostructures with tunable sizes, morphologies and structures. Moreover, their excellent photocatalytic activities and heavy metal Cr(VI) removal capacities should be significantly valuable for further practical application in water treatment.

Acknowledgments

This work was supported by the National Natural Science Foundation of China (Grant No. 21171136), the Program for New Century Excellent Talents in University (NCET-09-0136), Open Research Fund of State Key Laboratory of Advanced Technology for Materials Synthesis and Processing (Wuhan University of Technology, 2013-KF-6) and the Natural Science Foundation of Hubei Province (2011CDB219).

Appendix A. Supplementary material

Supplementary data associated with this article can be found, in the online version, at <http://dx.doi.org/10.1016/j.jcis.2013.07.068>.

References

- [1] Y.-E. Miao, R. Wang, D. Chen, Z. Liu, T. Liu, *ACS Appl. Mater. Interfaces* 4 (2012) 5353.
- [2] C. Chen, P. Gunawan, R. Xu, *J. Mater. Chem.* 21 (2011) 1218.
- [3] F. Qin, G. Li, H. Xiao, Z. Lu, H. Sun, R. Chen, *Dalton Trans.* 41 (2012) 11263.
- [4] L. Zhang, H. Wang, Z. Chen, P.K. Wong, J. Liu, *Appl. Catal., B – Environ.* 106 (2011) 1.
- [5] C. Pan, Y. Zhu, *J. Mater. Chem.* 21 (2011) 4235.
- [6] F. Qin, G. Li, R. Wang, J. Wu, H. Sun, R. Chen, *Chem. Eur. J.* 18 (2012) 16491.
- [7] F. Qin, R. Wang, G. Li, F. Tian, H. Zhao, R. Chen, *Catal. Commun.* (2013), <http://dx.doi.org/10.1016/j.catcom.2013.07.039>.
- [8] R. Boldt, M. Kaiser, D. Köhler, F. Krumeich, M. Ruck, *Nano Lett.* 10 (2010) 208.
- [9] L. Ye, L. Tian, T. Peng, L. Zan, *J. Mater. Chem.* 21 (2011) 12479.
- [10] Z. Sun, S. Liufu, X. Chen, L. Chen, *Chem. Commun.* 46 (2010) 3101.
- [11] R. Li, F. Zhang, D. Wang, J. Yang, M. Li, J. Zhu, X. Zhou, H. Han, C. Li, *Nat. Commun.* 4 (2013) 1432.
- [12] K.E. Kweon, G.S. Hwang, *Phys. Rev. B* 87 (2013) 205202.
- [13] M. Guan, C. Xiao, J. Zhang, S. Fan, R. An, Q. Cheng, J. Xie, M. Zhou, B. Ye, Y. Xie, *J. Am. Chem. Soc.* 135 (2013) 10411.
- [14] L. Zhang, T. Xu, X. Zhao, Y. Zhu, *Appl. Catal., B – Environ.* 98 (2010) 138.
- [15] J. Jiang, K. Zhao, X. Xiao, L. Zhang, *J. Am. Chem. Soc.* 134 (2012) 4473.
- [16] J. Xiong, G. Cheng, Z. Lu, J. Tang, X. Yu, R. Chen, *CrystEngComm* 13 (2011) 2381.
- [17] G. Li, Y. Ding, Y. Zhang, Z. Lu, H. Sun, R. Chen, *J. Colloid Interface Sci.* 363 (2011) 497.
- [18] X. Zhang, Z. Ai, F. Jia, L. Zhang, *J. Phys. Chem. C* 112 (2008) 747.
- [19] Z. Ai, W. Ho, S. Lee, L. Zhang, *Environ. Sci. Technol.* 43 (2009) 4143.
- [20] H. Cheng, B. Huang, P. Wang, Z. Wang, Z. Lou, J. Wang, X. Qin, X. Zhang, Y. Dai, *Chem. Commun.* 47 (2011) 7054.
- [21] J. Xiong, G. Cheng, G. Li, F. Qin, R. Chen, *RSC Adv.* 1 (2011) 1542.
- [22] X. Xiao, W.-D. Zhang, *J. Mater. Chem.* 20 (2010) 5866.
- [23] K. Liang, J. Liang, S. Wang, J. Liu, K. Ren, X. Zheng, H. Luo, Y. Peng, X. Zou, X. Bo, J. Li, X. Yu, *Cryst. Growth Des.* 12 (2012) 793.
- [24] M. Rycenga, X. Xia, C.H. Moran, F. Zhou, D. Qin, Z.Y. Li, Y. Xia, *Angew. Chem. Int. Ed.* 50 (2011) 5473.
- [25] G. Li, F. Qin, H. Yang, Z. Lu, H. Sun, R. Chen, *Eur. J. Inorg. Chem.* 2012 (2012) 2508.
- [26] M. Shang, W. Wang, L. Zhang, *J. Hazard. Mater.* 167 (2009) 803.
- [27] H. Peng, C.K. Chan, S. Meister, X.F. Zhang, Y. Cui, *Chem. Mater.* 21 (2009) 247.
- [28] J. Henle, P. Simon, A. Frenzel, S. Scholz, S. Kaskel, *Chem. Mater.* 19 (2007) 366.
- [29] J. Geng, W.-H. Hou, Y.-N. Lv, J.-J. Zhu, H.-Y. Chen, *Inorg. Chem.* 44 (2005) 8503.
- [30] I. Bilecka, M. Niederberger, *Nanoscale* 2 (2010) 1358.
- [31] M.B. Mohamed, K.M. AbouZeid, V. Abdelsayed, A.A. Aljarash, M.S. El-Shall, *ACS Nano* 4 (2010) 2766.
- [32] C.-Y. Cao, W. Guo, Z.-M. Cui, W.-G. Song, W. Cai, *J. Mater. Chem.* 21 (2011) 3204.
- [33] S. Kundu, L. Peng, H. Liang, *Inorg. Chem.* 47 (2008) 6344.
- [34] M. Baghbanzadeh, L. Carbone, P.D. Cozzoli, C.O. Kappe, *Angew. Chem. Int. Ed.* 50 (2011) 2.
- [35] Y. Yan, S. Sun, Y. Song, X. Yan, W. Guan, X. Liu, W. Shi, *J. Hazard. Mater.* 250–251 (2013) 106.
- [36] L.-S. Zhong, J.-S. Hu, A.-M. Cao, Q. Liu, W.-G. Song, L.-J. Wan, *Chem. Mater.* 19 (2007) 1648.
- [37] Y.-S. Luo, W.-D. Zhang, X.-J. Dai, Y. Yang, S.-Y. Fu, *J. Phys. Chem. C* 113 (2009) 4856.
- [38] L. Ye, L. Zan, L. Tian, T. Peng, J. Zhang, *Chem. Commun.* 47 (2011) 6951.
- [39] X. Han, M. Jin, S. Xie, Q. Kuang, Z. Jiang, Y. Jiang, Z. Xie, L. Zheng, *Angew. Chem. Int. Ed.* 48 (2009) 9180.
- [40] Z.-Y. Jiang, Q. Kuang, Z.-X. Xie, L.-S. Zheng, *Adv. Funct. Mater.* 20 (2010) 3634.
- [41] J. Zhang, F. Shi, J. Lin, D. Chen, J. Gao, Z. Huang, X. Ding, C. Tang, *Chem. Mater.* 20 (2008) 2937.
- [42] M.L. Huang, Q. Zhu, *Comp. Mater. Sci.* 46 (2009) 1076.
- [43] C. Lizandara-Pueyo, S. Siroky, M.R. Wagner, A. Hoffmann, J.S. Reparaz, M. Lehmann, S. Polarz, *Adv. Funct. Mater.* 21 (2011) 295.
- [44] J. Yu, G. Wang, B. Cheng, M. Zhou, *Appl. Catal., B – Environ.* 69 (2007) 171.
- [45] Y. Li, J. Liu, X. Huang, G. Li, *Cryst. Growth Des.* 7 (2007) 1350.
- [46] F. Amano, A. Yamakata, K. Nogami, M. Osawa, B. Ohtani, *J. Am. Chem. Soc.* 130 (2008) 17650.
- [47] M. Shang, W. Wang, H. Xu, *Cryst. Growth Des.* 9 (2008) 991.
- [48] X. Chang, M.A. Gondal, A.A. Al-Saadi, M.A. Ali, H. Shen, Q. Zhou, J. Zhang, M. Du, Y. Liu, G. Ji, *J. Colloid Interface Sci.* 377 (2012) 291.
- [49] S.S. Liu, Y.Z. Chen, L. De Zhang, G.M. Hua, W. Xu, N. Li, Y. Zhang, *J. Hazard. Mater.* 190 (2011) 723.
- [50] P.A. Kumar, S. Chakraborty, *J. Hazard. Mater.* 162 (2009) 1086.
- [51] L.-S. Zhong, J.-S. Hu, H.-P. Liang, A.-M. Cao, W.-G. Song, L.-J. Wan, *Adv. Mater.* 18 (2006) 2426.
- [52] J. Zhang, Y. Li, J. Zhou, D. Chen, G. Qian, *J. Hazard. Mater.* 205–206 (2012) 111.
- [53] X.-Y. Yu, T. Luo, Y. Jia, R.-X. Xu, C. Gao, Y.-X. Zhang, J.-H. Liu, X.-J. Huang, *Nanoscale* 4 (2012) 3466.